AGU ADVANCING EARTH AND SPACE SCIENCES

JGR Space Physics

Key Points:

- Chorus waves exponentially decay with a timescale on the order of an hour in the quiet period following substorms
- This decay timescale varies based on magnetic local time, magnetic latitude, and wave frequency
- Lower-band chorus waves between 21 and 5 magnetic local time decay with a similar timescale to energetic pulsating aurora electrons after substorms

Substorm Driven Chorus Waves: Decay Timescales and Implications for Pulsating Aurora

Riley N. Troyer[1] , Allison N. Jaynes[1] , David P. Hartley[1] , Nigel P. Meredith[2] , Man Hua[3], and Jacob Bortnik[3]

[1]Department of Physics and Astronomy, University of Iowa, Iowa City, IA, USA, [2]British Antarctic Survey, Natural Environment Research Council, Cambridge, UK, [3]University of California, Los Angeles, Los Angeles, CA, USA

Abstract Energetic electron precipitation (EEP) associated with pulsating aurora can transfer greater than 30 keV electrons from the outer radiation belt region into the upper atmosphere and can deplete atmospheric ozone via collisions that produce NOx and HOx molecules. Our knowledge of exactly how EEP occurs is incomplete. Previous studies have shown that pitch angle scattering between electrons and lower-band chorus waves can cause pulsating aurora associated with EEP and that substorms play an important role. In this work, we quantify the timescale of chorus wave decay following substorms and compare that to previously determined timescales. We find that the chorus decay e-folding time varies based on magnetic local time (MLT), magnetic latitude, and wave frequency. The shortest timescales occur for lower-band chorus in the 21 to 9 MLT region and compares, within uncertainty, to the energetic pulsating aurora timescale of Troyer et al. (2022, https://doi.org/10.3389/fspas.2022.1032552) for energetic pulsating aurora. We are able to further support this connection by modeling our findings in a quasi-linear diffusion simulation. These results provide observations of how chorus waves behave after substorms and add additional statistical evidence linking energetic pulsating aurora to substorm driven lower-band chorus waves.

1. Introduction

The outer Van Allen radiation belt is a region of space surrounding Earth, usually between $3 < L < 7$, that is filled with energetic electrons (Baker et al., 2013). These particles are trapped in the magnetic mirror created by the planet's approximate dipole magnetic field. During periods of low magnetic activity, charged particles are generally stably trapped and $\overline{E} \times \overline{B}$, gradient, and curvature drift around the planet (Roederer, 1970). However, there are several processes that can perturb these populations, causing them to precipitate into the atmosphere. In this study, we focus on the interaction between the energetic electrons and electromagnetic chorus waves. This interaction can precipitate energetic electrons into the atmosphere. Energetic electron precipitation (EEP) is an important dynamic to the magnetosphere-ionosphere-thermosphere coupled system (Lam et al., 2010). It represents a significant transfer of energy from magnetosphere to upper atmosphere and can result in ozone depletion (Turunen et al., 2016; Verronen et al., 2021). Pulsating aurora is a visual manifestation of the precipitating electrons and can be an excellent way to study EEP (e.g., Bland et al., 2021; Miyoshi et al., 2021, and others). There are still many unknowns in the process that produces EEP and pulsating aurora (Lessard, 2013; Partamies et al., 2022). In this work, we provide additional statistical evidence for substorm driven lower-band chorus waves as a source of energetic pulsating aurora. We do this by measuring chorus decay e-folding times after substorms and comparing them to known pulsating aurora energy decay timescales.

Chorus waves are an important feature of the outer Van Allen radiation belt region and drive many of this region's dynamics (Hua, Bortnik, Kellerman, et al., 2023; Hua, Bortnik, Spence, & Reeves, 2023; Summers et al., 1998). They are characterized by frequency, which typically ranges between the electron cyclotron frequency (f_{ce}) and one tenth of f_{ce}. There is a clear gap at one half f_{ce}, likely due to Landau resonance, such that lower-band chorus waves (LBC) occur between $0.1 f_{ce}$ and $0.5 f_{ce}$ while upper-band chorus waves (UBC) occur between $0.5 f_{ce}$ and f_{ce} (Bortnik et al., 2006; J. Li et al., 2019). In some cases low-frequency chorus can extend to $0.05 f_{ce}$ or lower (W. Li et al., 2013; Meredith et al., 2014). For our analysis we did not consider low-frequency chorus. Chorus waves are named for their resemblance to the sound of birds chirping caused by sub-second rising and falling tones in their frequency distributions (Isted & Millington, 1957; Tsurutani & Smith, 1974). In addition to the sub-second timescales, chorus waves can also be modulated on the order of seconds (Jaynes et al., 2015). Studies have directly linked modulations over seconds in the chorus power spectral density and electron flux in the chorus region to

instance of pulsating aurora, where an intensification corresponds to the brightening of an auroral patch (Jaynes et al., 2013; Kasahara et al., 2018; Nishimura et al., 2011). Due to the difficulty in connecting chorus activity to ground observations, these studies have only been able to analyze a handful of events.

Pulsating aurora are a common subset of diffuse-like aurora. They appear as an uncoordinated symphony of dim auroral patches that blink on and off across wide portions of the sky. The period of this blinking can range up to around 20 s. Individual patches can be remarkably varied with differing periods, shapes, and sizes typically between 10 and 100s of kilometers (Johnstone, 1978; Lessard, 2013). Pulsating aurora often develop near the end of a substorm display and can continue for hours after (Jones et al., 2011). There also is a relation between greater energy flux and closer temporal proximity to the substorm (Hosokawa & Ogawa, 2015; Oyama et al., 2017; Troyer et al., 2022). Substorms are characterized by a rapid dipolarization of Earth's nightside magnetic field that accelerates and injects electrons into the inner magnetosphere (Akasofu, 1966). Some of these electrons accelerate directly into the atmosphere, causing discrete aurora (Korth et al., 2014; Schroeder et al., 2021). Others are injected into the radiation belt region and can drive wave activity (Chepuri et al., 2023; Tsurutani & Smith, 1974). Ground-based magnetometers can detect substorms as an enhancement of the auroral electrojet and report this in the AE index (Newell & Gjerloev, 2011).

While a correlation does exist between LBC waves and pulsating aurora for certain events, it is still an open question as to how statistically significant this relationship is (Borovsky & Partamies, 2022; Lessard, 2013). That being said, there are known, indirect, statistical links between the two. For instance, both LBC and pulsating aurora occur most frequently and with the strongest intensity between 3 and 6 MLT (Jones et al., 2011; Meredith et al., 2020; Oguti et al., 1981). Additionally, pulsating aurora frequently have significant energy contributions from 10 to 100s of keV electrons, which is the resonant energy range for lower-band chorus (Nishimura et al., 2011; Tesema et al., 2020; Troyer et al., 2022). In this work we add to that evidence by showing that lower-band chorus and pulsating aurora have similar decay timescales after substorms.

A proposed process for this interaction is Doppler-shifted cyclotron resonance between 10s of keV electrons and lower-band chorus, which can simultaneously drive wave growth and pitch angle scatter electrons (Brice, 1964; Miyoshi et al., 2020; Trakhtengerts et al., 2004). Therefore, assuming pitch angle scattered electrons are responsible for pulsating aurora, an e-folding decay time in the auroral electron flux should correspond to a proportional decay timescale in the resonant wave power. Troyer et al. (2022) found such a timescale for $\geq$30 keV electrons associated with pulsating aurora. They found that the differential energy flux from these electrons decayed after substorms with a timescale of just under an hour, suggesting that substorms are a primary driver of pulsating aurora EEP. Complementing this, Meredith et al. (2000) found a similar timescale when looking at post-substorm decay of chorus electric field amplitudes from the CRRES spacecraft. However, they were only able to measure approximately 15 data points to calculate this decay, thus there is a need for a follow up study to expand on and confirm these results. We hypothesize that energetic electrons injected into the outer radiation belt region during substorms drive chorus waves, and that pitch angle scattering from this interaction causes pulsating aurora. We provide evidence toward that hypothesis by expanding on Meredith et al. (2000) using the more recent and expansive Van Allen Probes data set. In doing so, we confirmed that lower-band chorus waves decay after substorms with a similar timescale to pulsating aurora. We also discovered that this decay timescale depends on magnetic local time (MLT), magnetic latitude (MLAT), and wave frequency. Our quantified decay timescales add statistical evidence linking chorus waves, substorms, and pulsating aurora. Our work differs from previous studies looking at substorms, chorus waves, and EEP, such as that of Rodger et al. (2022), because of our specific focus on pulsating aurora. While there is still much work to be done in this area, a rigorous quantitative link between these phenomena and pulsating aurora would provide a means to study the outer radiation belt through all-sky camera observations.

2. Data

2.1. Electric and Magnetic Fields

Our primary data set is from the Electric and Magnetic Field Instrument Suite and Integrated Science (EMFISIS) instruments aboard the Van Allen Probes. The Van Allen Probes were two identical spacecraft that orbited through the planet's radiation belt regions between 2012 and 2019 (Mauk et al., 2013). EMFISIS uses a tri-axial fluxgate magnetometer (MAG) and a tri-axial search coil magnetometer (MSC) to measure DC and wave magnetic fields

respectively (Kletzing et al., 2013a). EMFISIS also takes an analog electric field signal from the Electric Fields and Waves (EFW) experiment to measure the wave electric field (Wygant et al., 2013). The collective wave electric and magnetic field measurements are called the Waves experiment and cover the frequency range from 10 Hz up to 12 kHz. In survey mode, the Waves experiment provides a 6-s resolution power spectral density produced from 0.468-s waveforms for both the electric and magnetic fields in three orthogonal directions. We used the total electric/magnetic power spectral density, which is a sum of all three components.

A property of the double probe electric field sensors on the Van Allen Probes is that they become electrically coupled to the local plasma. To account for this, we use the sheath-corrected electric field measurements that provide an adjustment based on local electron density (Hartley et al., 2022). In addition, the electric field measurements contain noisy frequency bands at 1781 Hz and 3555 Hz, so we omitted these data for our analysis. We are more confident in the magnetic field measurements and used these for most of our findings. For the specific EMFISIS data we used please see Kletzing et al. (2013b).

2.2. Post-Substorm Identification

To detect substorm activity we used the SuperMAG collaboration's 1-min SuperMAG auroral electrojet (SME) index (Gjerloev, 2012a, 2012b). This index is designed to replicate the AE index using at least 100 of the Super-MAG magnetometers. Similar to AE, SME is measured in nT with larger positive values corresponding to a stronger auroral electrojet (Newell & Gjerloev, 2011).

The AE index, and thus SME, correlates well with particle injections in the inner magnetosphere (Meredith et al., 2000). These injections are linked with substorms and reconnection in the magnetotail (Chepuri et al., 2023; DeForest & McIlwain, 1971). We looked at the behavior of chorus wave events during the quiet period following an injection. We identified these events with the following process:

1. Smooth the SME index with a rolling average of 6 min.
2. Identify periods where the smoothed SME index stayed below 150 nT for at least 10 min.
3. From these periods, select only those that were preceded by an enhancement in smoothed SME of >250 nT.

Our threshold of <150 nT, representing the start of a quiet period, is based on Meredith et al. (2000). Additionally, we found that >250 nT was sufficient to identify true enhanced periods instead of times with just a slightly higher SME value. We performed our search in this order because the number of times that SME goes above 250 nT is much greater than the number of times where is was below 150 nT for more than 10 min.

We also measured the approximate substorm injection period length. We define this as the time from when the smoothed SME went above 250 nT to when it dropped below 150 nT. Using this definition, our median injection length from 6241 events was 1.73 ± 0.02 hr. However, these values should be taken with a grain of salt as they assume that an enhanced SME corresponds to a continuous injection event. We've included plots of our injection period and quiet period length distributions in Figure S4 in Supporting Information S1.

2.3. Chorus Selection

Within the quiet periods after injections, we further limited our search to the outer radiation belt region ($3.8 \leq L \leq 6$) and considered all MLTs, and all magnetic latitudes sampled by the Van Allen Probes ($-20° \leq \text{MLAT} \leq 20°$). Our L range is smaller than the typical description of the outer radiation belt, because we chose it to match that of Meredith et al. (2000).

To identify chorus we determined the local electron cyclotron frequency (f_{ce}) using the magnetic field amplitude from the EMFISIS flux gate magnetometer (MAG) and the equation $f_{ce}[\text{Hz}] = \left| \vec{B}[\text{nT}] \right| \times 28$. We then used local f_{ce} to select chorus from the power spectral density data. To qualify as a measurement of LBC or UBC we required that the maximum magnetic field power spectral density over the respective frequency range be $\geq 10^{-7}$ nT^2/Hz (Hartley et al., 2019). To reduce hiss noise, we ensured that the probes were outside the plasmasphere by limiting our measurements to times when the electron density was less than the smaller of $10 \times (6.6/L)^4$ or 50 cm^{-3} (Aryan et al., 2022; Lawrence et al., 1999; Sheeley et al., 2001). Note that in Sheeley et al. (2001) the equation is written as $10 \times (6.6/L)^{-4}$, but we believe that this is a typograhpical mistake. Subsequent studies have implemented the equation we used to good results and it is intuitive that the density threshold would decrease at larger L values
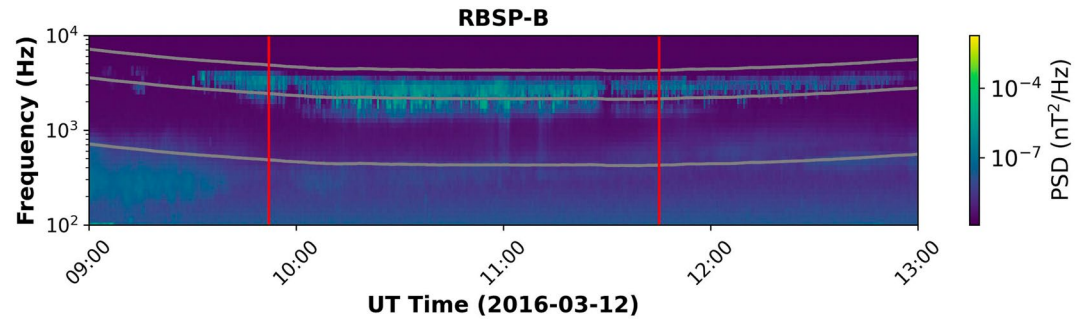
Figure 1. An example of chorus wave measurements from the EMFISIS MAG instrument on the RBSP-B probe. The gray lines indicate f_{ce}, $f_{ce}/2$, and $f_{ce}/10$. The red lines indicate the period that falls within a quiet period following a substorm and thus the measurements that were included in our study.

(W. Li et al., 2015). For the density, we used the estimated values provided by EMFISIS. We did not use any additional metrics to identify chorus, but these criteria have been successfully used in the past (Meredith et al., 2012, 2020).

3. Analysis

Our base data set includes 224,165 chorus measurements from the EMFISIS instrument. Each measurement consists of a frequency integrated LBC and/or UBC wave power derived from a 0.468-s waveform. These measurements have a 6-s resolution and are each associated with a probe location, and a time since the start of the respective quiet period. Figure 1 shows a series of chorus measurements on 2016-03-12 from the EMFISIS MAG instrument on RBSP-B. The gray lines indicate f_{ce}, $f_{ce}/2$, and $f_{ce}/10$. The red lines indicate the period that falls within a quiet period following a substorm. Each vertical slice represents one chorus measurement. We can use this data set to better understand how chorus waves behave after a substorm.

3.1. Timescale Calculation

We further subdivided our data set by magnetic local time and magnetic latitude, as described in Sections 3.2 and 3.3. For each of these subdivisions we got a distribution of chorus wave power measurements that depend on time since the start of a quiet period. We further divided this into 1-min slices. The resulting distributions are heavily right skewed, meaning that the measurement range extends several orders of magnitude higher than the distribution peak. We calculated the most likely value by performing the following operation, which transformed the data into a normal distribution.

$$Y_{\text{normal}} = \log_{10}\left\{ \log_{10}(X_{\text{skewed}}) + \left|\min\left[\log_{10}(X_{\text{skewed}})\right]\right| + 1 \right\} \tag{1}$$

We then calculated a best fit normal distribution and the associated mean of the transformed data. Finally, we reversed the transformation to arrive at our most likely chorus power measurement. While this process is more involved than taking a simple mean or median, we found it to be a much better and rigorous representation of the individual distributions. We did this for the first 60 1-min slices. Using the natural log of these 60 data points we conducted a least squares linear fit to determine the exponential decay. To determine the validity of a linear fit we performed several statistical tests to assess the homoscedasticity of our data. The results of these, including QQ plots, a histogram of residuals, and a scatter plot of residuals versus predicted values, are in Figures S1 and S2 in Supporting Information S1.

Homoscedasticity refers to data points which have similar variances along the independent variable. If the data set is not homoscedastic a linear fit is not valid. A QQ plot refers to a quantile–quantile plot, which should be roughly linear for a homoscedastic data set.

We estimated the error in our linear fit by bootstrapping (Johnson, 2001). To bootstrap, we resampled our 60 values 10,000 times, with replacement, and found the slope for these new distributions. We then used the standard deviation of these 10,000 resampled slopes as the associated error.
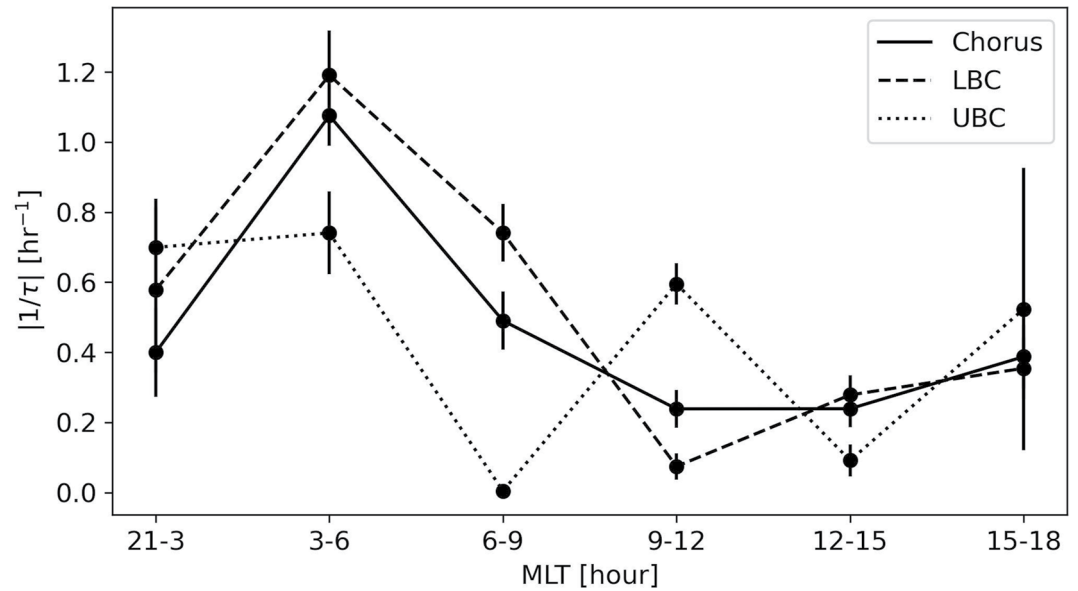
Figure 2. The inverse of magnetic field wave power timescales (decay rate) for the entire chorus range (solid), LBC (dashed), and UBC (dotted) versus MLT. We combined the region 21 to 24 and 0 to 3 MLT and omitted 18 to 21 MLT due to statistical limitations.

3.2. Variations With Magnetic Local Time (MLT)

We subdivide our data set into the following regions of MLT: 21 to 3 (11,349 measurements), 3 to 6 (17,925), 6 to 9 (22,708), 9 to 12 (20,550), 12 to 15 (27,704), and 15 to 18 (11,395). We excluded 18 to 21 (1,412 measurements) due to limited chorus observations. We also and combined 21 to 24 (1,890) with 0–3 (9,459) into a near midnight bin, again due to limited observations. While it isn't the purpose of this study, it is worth noting that our statistical distribution does roughly agree with the previous understanding of chorus occurrence and wave power in relation to MLT (W. Li et al., 2016; Meredith et al., 2020). Occurrence and wave power peaks post-midnight and are lowest between 18 and 21 MLT.

For each MLT region we processed the data as described in Section 3.1. This resulted in a fitted exponential decay in form of

$$B = B_0 \, e^{-t/\tau} \tag{2}$$

where t is the time since the start of a quiet period and B_0 is the magnetic wave power at $t = 0$. Figure 2 shows how the inverse of these decay timescales (the decay rates) vary across our MLT regions. We chose to plot $|1/\tau|$ to better distinguish between differences in decay rates. We split the decays into data that was integrated over the full chorus frequency range (solid), LBC frequency range (dashed), and UBC frequency range (dotted) to visualize the differences between the different chorus types. Using Figure 2 we find that the timescale is shorter in the night to early morning regions, with longer timescales on the dayside. The shortest timescales occur between 3 and 6 MLT with the LBC timescale about half that of the UBC. This region of MLT also happens to be the most common region for pulsating aurora (Kvifte & Pettersen, 1969), which we will discuss in Section 3.5.

3.3. Variations With Magnetic Latitude (MLAT)

In Figure 2, we saw that decay timescales on the nightside through dawn were shorter than on the dayside. We are also interested in investigating how our data varies with magnetic latitude (MLAT). We define MLAT as the angle, at a constant L value, away from the magnetic equator. To look at changes with MLAT, we divided our data into two MLT bins: 21 to 9, and 9 to 18. We would expect that close to the injection region (21–9 MLT), chorus would be more intense, but also damped quicker away from the equator due to the presence of Landau resonant electrons with energies on the order of 1 keV (Bortnik et al., 2007). Further away from the injection (9–18 MLT) we would expect less damping at higher latitudes as the ~1 keV electrons will be lost faster than the ~30 keV
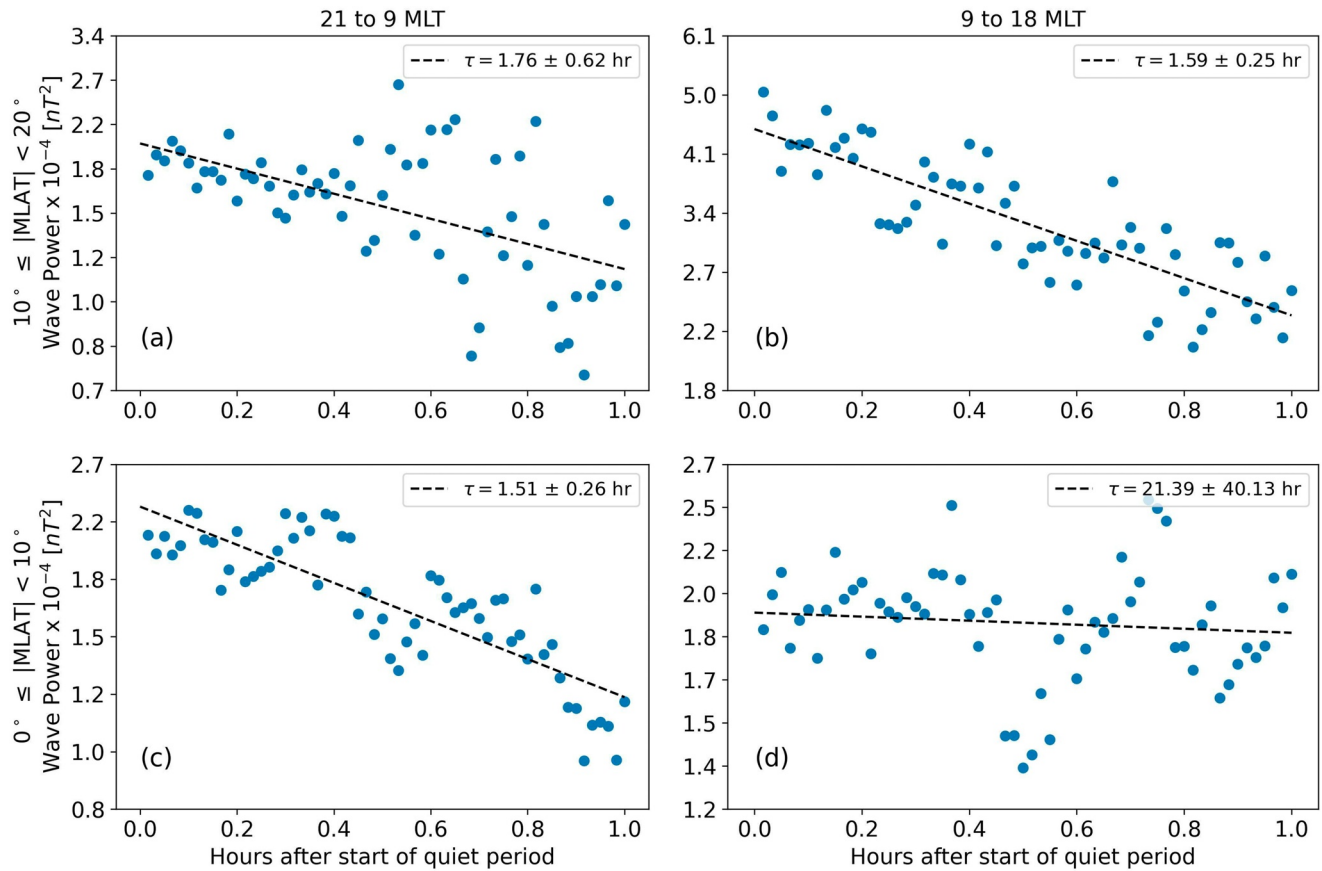
Figure 3. Statistical behavior, during the quiet period following substorms, of magnetic chorus wave power. The left (right) column of figures shows the behavior in the 21 to 9 MLT (9–18 MLT) region. The bottom (top) row of figures shows the behavior for 0°–10° (10°–20°) MLAT. The blue scatter points represent the distribution peak for the proceeding 1 min of chorus power measurements. The dashed line is a linear regression model of the scatter points.

ones responsible for chorus. In Figure 3, we compare the decay timescales between these two regions and for 0°–10° and 10°–20° MLAT. Here the blue scatter points are the distribution peaks for the proceeding 1 min of measurements and the dashed black lines are the least squares fits to these values. In this figure, we see that the behavior roughly agrees with what we would expect. During the daytime, wave power is damped less and thus is larger at higher latitudes. We also see that the shortest decay timescales occur near the equator in the 21 to 9 MLT region. The decay timescale at higher latitudes, in this region, is slightly longer and not as uniform. This is also evident in the our statistical tests (see Figure S1 in Supporting Information S1), where the fit at higher latitudes was worse. In the 9 to 18 MLT region the opposite is true. At high latitudes the timescale is more uniform and shorter than near the equator. Again, this carried through to our statistical tests. However, we found that near the daytime equator, for times >1 hr, there is a uniform decay with a timescale of 1.84 ± 0.45 hr, see Figure S4 in Supporting Information S1. We do not have a rigorous explanation for these variations, but it is interesting to note that higher latitude waves, at a given L, may originate from higher L shells near the equator (Bortnik et al., 2008). Drifts at higher L shells, for a given energy, are faster, thus could be responsible for the shorter response time that we see in Panel (b) compared to Panel (d).

3.4. Comparison With Meredith et al. (2000)

Meredith et al. (2000) used electric field measurements from the CRRES spacecraft and found a chorus amplitude decay timescale after injections of 1.1 ± 0.2 hr in the region 21 to 6 MLT and $3.8 \leq L < 6$. This would correspond to a 0.55 hr decay in the wave power. To compare our data to this value we used the EMFISIS electric field measurements. We then found the electric wave power decay in the region 21 to 6 MLT, $3.8 \leq L \leq 6$, and $\pm 5°$ MLAT, and fit our decay to the first 1 hr. Given these parameters we find that the electric wave power decays with
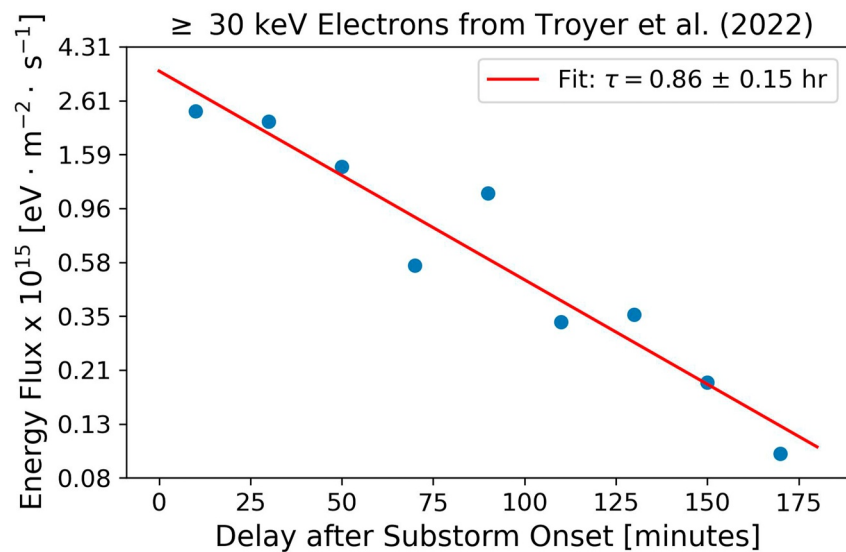
Figure 4. Expanded figure from Troyer et al. (2022) showing the decay of ≥30 keV pulsating aurora electrons after substorms. The blue scatter points indicate the distribution peak of the surrounding 20 min of measurements and the red line is the best fit exponential decay.

an e-folding time of 0.66 ± 0.11 hr, which agrees well with the previous results. While our timescales are similar, there are several key differences between the studies. One is the statistical sample size as Meredith et al. (2000) was working with <20 data points compared to our much larger data set. A second is the method of identifying injection periods. Our automated identification allows us to analyze the large EMFISIS data set, but may include weaker injection periods that a human identifier would overlook.

3.5. Comparison With Pulsating Aurora and Troyer et al. (2022)

Troyer et al. (2022) found that the contribution to the total energy flux from ≥30 keV electrons during pulsating aurora decayed on the order of 1 hour after substorms. Figure 4 shows an extension of the decay plot from Troyer et al. (2022). We fit an exponential to the measurements using the same process as outlined in Section 3.1, but for these data the transformation that produced a normal distribution was: $Y_{\text{normal}} = \log_{10}(X_{\text{skewed}})$. In the plot, the blue scatter points are the distribution peaks for the surrounding 20 min of measurements and the red line is the best fit exponential. Here we see that ≥30 keV pulsating aurora electrons decayed after substorms with an e-folding time of 0.86 ± 0.16 hr. To compare our data to these findings we considered the difference between chorus types as LBC has been directly linked to pulsating aurora, while UBC is more commonly associated with the less energetic non-pulsating diffuse aurora (Meredith et al., 2009; Nishimura et al., 2010). This is not surprising as LBC waves resonate with higher energy electrons (>5 keV near the loss cone) compared to UBC waves (<5 keV) (Ni et al., 2008). In Figure 2, we can see that during the most common time for pulsating aurora (3–6 MLT) LBC decayed with a shorter timescale than UBC (Jones et al., 2011; Kvifte & Pettersen, 1969). Figure 5 is a more direct comparison to Troyer et al. (2022). Here we look at the difference between LBC and UBC in the region: 21 to 5 MLT, 3.8 < L < 6, and −20° to 20° MLAT. Again, LBC decayed with a shorter timescale compared to UBC. For LBC the e-folding time is between 0.89 and 1.71 hr, considering uncertainty. For the ≥30 keV electrons from Figure 4 the e-folding time is between 0.70 and 1.02 hr. This agrees, within uncertainty, to the timescale of LBC. However, the timescale for UBC is also close to agreeing. Thus, while these results add further statistical evidence linking LBC and pulsating aurora, more work is needed to understand the specific contributions from LBC versus UBC.

3.6. Simulation

As another test, we modeled the system using the quasi-linear, drift-averaged, diffusion simulation described in Hua et al. (2022). To calculate the diffusion coefficients, we set the wave power in the 21 to 3, 3 to 6, and 6 to 9 MLT regions to
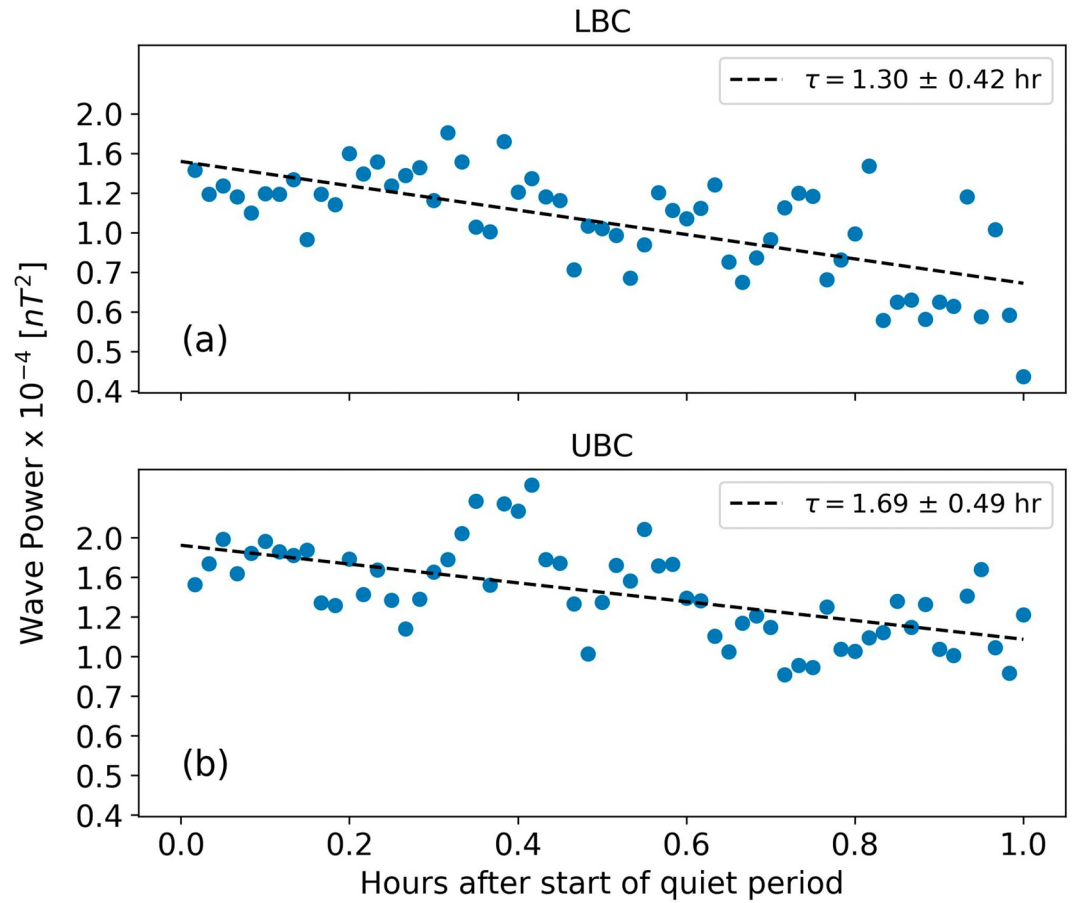
Figure 5. Statistical behavior of magnetic wave power, during the quiet period following substorms, from the LBC (a) and UBC (b) frequency ranges. Data in the figure is from the region 21 to 5 MLT, $3.8 < L < 6$, and $-20°$ to $20°$ MLAT. The blue scatter points represent the distribution peak for the proceeding 1 min of chorus power measurements. The dashed line is a linear regression model of the scatter points.

$$B_w(t) = B_0\, e^{-t/\tau} \tag{3}$$

where t is the simulation time, τ is the decay e-folding time that we measured for the specific region, and B_0 is the max wave intensity in the region taken from Meredith et al. (2020) at $L = 5$ and $100 \leq AE < 300$ nT. In all other regions we let $B_w(t) = B_0$. The simulation requires a specific L value as input and we chose $L = 5$ because it falls within the outer radiation belt region.

We used the values of Meredith et al. (2020) for B_0 because they provide a large sample size over our MLT bins and have been used in similar simulations (Hua, Bortnik, Kellerman, et al., 2023; Hua et al., 2022). Although it wasn't the primary focus of this work, we can also derive B_0 from our data. Doing so, we find that it differs from Meredith et al. (2020). For instance, we see a peak B_0 on the order of 20 pT in the 3 to 6 MLT region, while for $AE < 100$ nT, Meredith et al. (2020) found it to be on the order of 40–50 pT. We believe this is due to different averaging techniques. Meredith et al. (2020) used an arithmetic mean, while we used a geometric mean because the chorus power distribution is spread over multiple orders of magnitude. Using an arithmetic mean we get B_0 on the order of 40 pT.

Figure 6 summarizes the results of our simulation. Panel (a) shows how the initial electron energy distribution decays over the simulation. We report the electron distribution in units of spin-averaged flux as the Van Allen Probes ECT instrument would measure it (Boyd et al., 2019; Spence et al., 2013). We took the initial flux as measured by ECT from the 25 October 2016 storm event (Hua et al., 2022). In Panel (a) we've marked the region of electron loss (14–125 keV) with solid black lines. We've also marked 30 keV with a dashed red line to match
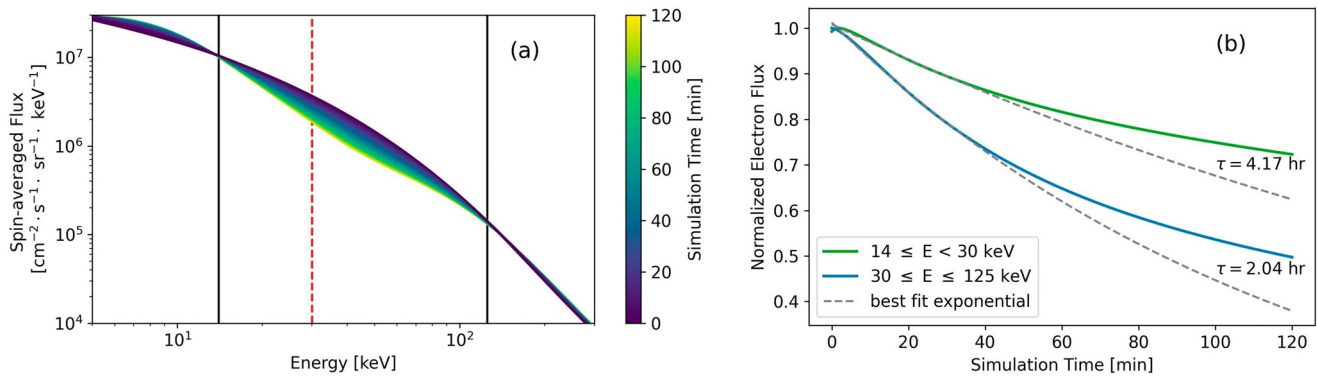
Figure 6. Results from our quasi-linear diffusion simulation of chorus waves. Panel (a) shows how the initial electron energy distribution decays over the simulation. The solid black lines indicate 14 and 125 keV and are the approximate bounds of electron loss. The dashed red line indicates 30 keV, which we define as the boundary between high and low energy electrons. Panel (b) shows the summed decay of low ($14\,\text{keV} \leq E < 30\,\text{keV}$) and high ($30\,\text{keV} \leq E \leq 125\,\text{keV}$) electrons within the region of electron loss. The solid lines indicate the normalized flux decays, while the dashed gray lines are the best fit exponentials, $\tau = 2.69$ hr and $\tau = 1.35$ hr respectively, for the first 30 min of the simulation.

the threshold of Troyer et al. (2022). Panel (b) shows the summed electron flux, in the region of electron loss, for low-energy electrons ($14\,\text{keV} \leq E < 30\,\text{keV}$) and high-energy electrons ($30\,\text{keV} \leq E \leq 125\,\text{keV}$).

Due to the drift-averaged nature of the simulation, we can't directly compare these decay times to timescales measured in a specific region of MLT, although they are on the same order of magnitude. For instance, electrons with 45 keV decay with the shortest timescale and have an e-folding time of 1.78 hr. This decay time will also vary depending on the peak chorus power, with higher power resulting in a shorter e-folding time. We can, however, investigate the relative differences between the higher and lower energy electrons. In Figure 6b, we see that, in the first 30 min of the simulation, the ≥30 keV electrons decay with an e-folding time of 2.04 hr, while for the <30 keV electrons the time is 4.17 hr. Clearly the flux of higher energy electrons from the radiation belt region decays with a shorter timescale compared to the lower energy electrons. Thus, after a substorm, we would expect to see a more dramatic change in the higher energy precipitating electrons as measured on the ground. That agrees well with Troyer et al. (2022), who showed that the post-substorm decay in energy flux during pulsating aurora was mainly due to a reduction in the ≥30 keV electrons, with the <30 keV electrons changing relatively little.

One point to note is that our simulation does not take into account the anomalous trapping effect, which moves low equatorial pitch angle electrons in the tens of keV energy range toward a higher pitch angle (Albert et al., 2022; Kitahara & Katoh, 2019). While this could be a possible explanation for the difference in ≥30 keV versus <30 keV electrons, we don't believe it would produce a significant change given that our starting magnetic field amplitudes, B_0, are in the 10s of pT.

4. Discussion

First order cyclotron resonance with injected energetic electrons is one proposed mechanism for chorus wave growth (Brice, 1964; Kennel & Petschek, 1966). In this process the electron interacts with the perpendicular electric field, causing it to transfer energy to the wave and reducing the pitch angle. To keep wave growth active the average velocity of the electrons perpendicular to the magnetic field must be greater than the average parallel velocity (Brice, 1964). Qualitatively, our results are consistent with this process. During injections, electrons typically enter the outer radiation belt region just before magnetic midnight (Gabrielse et al., 2014). They then gradient-curvature drift eastward, overtaking the slower, less energetic (a few to ∼30 keV) plasmasheet electrons. The interaction of these two populations can provide the anisotropies necessary for pitch angle scattering (Oguti, 1976). As time progresses the electron distribution, and correspondingly wave activity, will tend toward an equilibrium (Kennel & Petschek, 1966). Thus, chorus wave activity should have less time dependence further eastward (later MLT). This is what we see in Figure 2, with the shortest decay timescales between 3 and 6 MLT and the longest timescales in later MLT bins.

Performing a quantitative analysis of the decay timescale is more challenging and not something we attempt in this paper. To do so we would need to take several aspects of the system into consideration. One is the energy

dispersion due to gradient-curvature drift. Higher energy electrons will drift eastward at a faster rate, meaning the lower energy electrons will last longer in a particular MLT region. A second is the energy and pitch angle distribution of the injected electrons. The process that drives chorus growth simultaneously reduces the electron energy and pitch angle. After enough interactions an electron that was originally resonant will either precipitate into the atmosphere or lose enough energy that it is no longer resonant. A third is the temporal and spatial scale of the injection. For a longer and wider injection, by the time we take our measurement, the electron population will be spread over a larger region of MLT. We were able to estimate the median length of the injections as 1.73 ± 0.02 hr, but have no measure of the spatial extent. In Section 3.6 we were able to simulate an approximation of these events, but to understand the underlying physics we would need to specifically model the processes just after a substorm. While we did not perform that analysis, we hope that our measured decay timescales will provide a means to test future models.

As we showed in Section 3.5, the decay timescale is similar between LBC in the 21 to 5 MLT region and the energy flux of energetic pulsating aurora. However, this is not a smoking gun and our results should be considered as additional statistical evidence linking energetic pulsating aurora to chorus waves and substorms. Combined with prior studies, LBC certainly appear to play an important role in the formation of pulsating aurora, but the specific processes are likely more complicated than we've outlined here.

4.1. Magnetic and Electric Field Differences

To compare with Meredith et al. (2000) we also analyzed the electric wave power for our chorus measurements. Due to data quality, we believe the magnetic field analysis is more reliable and so chose to focus on it for our results. However, during our analysis, we did find several differences between the magnetic and electric decay timescales. The largest difference was in the region 21 to 3 MLT, where $\tau_{electric} < \tau_{magnetic}$, and for 3 to 6 MLT, where $\tau_{electric} > \tau_{magnetic}$. We've included Figure S3 in Supporting Information S1 to show this. We do not fully understand how this would occur, but there are two possibilities. One is wave normal angle of the chorus that, as W. Li et al. (2016) found, varies with MLT. Waves in the 3 to 6 MLT region are less field aligned (larger wave normal angle) than those close to midnight. They also found that waves with angles >40° tend to have weaker magnetic field power compared with angles <30°, while the electric field is comparable. However, this connection is highly speculative and we would need to conduct additional work to determine if it could cause our observed decay timescale differences.

5. Summary

We have confirmed, using a substantially larger data set, that chorus waves exponentially decay in the quiet period following a substorm. We further discovered that the timescale of this decay varies based on magnetic local time (MLT), magnetic latitude, and frequency range. The shortest decay times occurred for lower-band chorus waves between 21 and 9 MLT with a peak at 3 to 6 MLT. The lower-band chorus magnetic field power spectral density decays in the region 21 to 5 MLT with an e-folding time of 1.30 ± 0.41 hr. This compares, within uncertainty, with the 0.86 ± 0.16 hr timescale that Troyer et al. (2022) measured for ≥30 keV pulsating aurora electrons after substorms. We also modeled our findings in a quasi-linear diffusion simulation and found that ≥30 keV electrons decay with a timescale about half as long as the <30 keV population. These statistical decay timescales provide a valuable metric that can be used to track processes through the magnetosphere-ionosphere system and to test the validity of future models.

Data Availability Statement

The Van Allen Probe/EMFISIS data referenced in this paper is available at https://emfisis.physics.uiowa.edu/data/index (Kletzing et al., 2013b). The SME index referenced in this paper is available from SuperMAG: https://supermag.jhuapl.edu/indices/?fidelity=low&layers=SME.UL&start=2001-01-01T00%3A00%3A00.000Z&step=14400&tab=download (Gjerloev, 2012a).

References

Akasofu, S.-I. (1966). The auroral oval, the auroral substorm, and their relations with the internal structure of the magnetosphere. *Planetary and Space Science*, *14*(7), 587–595. https://doi.org/10.1016/0032-0633(66)90043-2

Albert, J. M., Artemyev, A., Li, W., Gan, L., & Ma, Q. (2022). Analytical results for phase bunching in the pendulum model of wave-particle interactions. *Frontiers in Astronomy and Space Sciences*, *9*, 971358. https://doi.org/10.3389/fspas.2022.971358

Aryan, H., Bortnik, J., Sibeck, D. G., & Hospodarsky, G. (2022). Global map of chorus wave sizes in the inner magnetosphere. *Journal of Geophysical Research: Space Physics*, *127*(3), e2021JA029768. https://doi.org/10.1029/2021JA029768

Baker, D. N., Kanekal, S. G., Hoxie, V. C., Henderson, M. G., Li, X., Spence, H. E., et al. (2013). A long-lived relativistic electron storage ring embedded in Earth's outer Van Allen belt. *Science*, *340*(6129), 186–190. https://doi.org/10.1126/science.1233518

Bland, E., Tesema, F., & Partamies, N. (2021). D-region impact area of energetic electron precipitation during pulsating aurora. *Annales Geophysicae*, *39*(1), 135–149. https://doi.org/10.5194/angeo-39-135-2021

Borovsky, J. E., & Partamies, N. (2022). What produces and what controls the spatial-temporal structuring of the magnetospheric chorus waves that create the pulsating aurora: An unsolved problem in need of new measurements. *Frontiers in Astronomy and Space Sciences*, *9*, 1059039. https://doi.org/10.3389/fspas.2022.1059039

Bortnik, J., Inan, U. S., & Bell, T. F. (2006). Landau damping and resultant unidirectional propagation of chorus waves. *Geophysical Research Letters*, *33*(3), L03102. https://doi.org/10.1029/2005GL024553

Bortnik, J., Thorne, R. M., & Meredith, N. P. (2007). Modeling the propagation characteristics of chorus using CRRES suprathermal electron fluxes: Propagation characteristics of chorus. *Journal of Geophysical Research*, *112*(A8), A08204. https://doi.org/10.1029/2006JA012237

Bortnik, J., Thorne, R. M., & Meredith, N. P. (2008). The unexpected origin of plasmaspheric hiss from discrete chorus emissions. *Nature*, *452*(7183), 62–66. https://doi.org/10.1038/nature06741

Boyd, A. J., Reeves, G. D., Spence, H. E., Funsten, H. O., Larsen, B. A., Skoug, R. M., et al. (2019). RBSP-ECT combined spin-averaged electron flux data product. *Journal of Geophysical Research: Space Physics*, *124*(11), 9124–9136. https://doi.org/10.1029/2019JA026733

Brice, N. (1964). Fundamentals of very low frequency emission generation mechanisms. *Journal of Geophysical Research*, *69*(21), 4515–4522. https://doi.org/10.1029/JZ069i021p04515

Chepuri, S. N. F., Jaynes, A. N., Turner, D. L., Gabrielse, C., Baker, D. N., Mauk, B. H., et al. (2023). A comparison of energetic particle energization observations MMS at and injections at Van Allen Probes. *Frontiers in Astronomy and Space Sciences*, *9*, 1033546. https://doi.org/10.3389/fspas.2022.1033546

DeForest, S. E., & McIlwain, C. E. (1971). Plasma clouds in the magnetosphere. *Journal of Geophysical Research*, *76*(16), 3587–3611. https://doi.org/10.1029/ja076i016p03587

Gabrielse, C., Angelopoulos, V., Runov, A., & Turner, D. L. (2014). Statistical characteristics of particle injections throughout the equatorial magnetotail. *Journal of Geophysical Research: Space Physics*, *119*(4), 2512–2535. https://doi.org/10.1002/2013JA019638

Gjerloev, J. W. (2012a). Sme index [Dataset]. Supermag Collaboration. Retrieved from https://supermag.jhuapl.edu/indices/?layers=SME.UL&fidelity=low&start=2001-01-29T18%3A30%3A00.000Z&step=14400&tab=download

Gjerloev, J. W. (2012b). The SuperMAG data processing technique. *Journal of Geophysical Research*, *117*(A9), A09213. https://doi.org/10.1029/2012JA017683

Hartley, D. P., Christopher, I. W., Kletzing, C. A., Kurth, W. S., Santolik, O., Kolmasova, I., et al. (2022). Quantifying the sheath impedance of the electric double probe instrument on the Van Allen Probes. *Journal of Geophysical Research: Space Physics*, *127*(5), e2022JA030369. https://doi.org/10.1029/2022JA030369

Hartley, D. P., Kletzing, C. A., Chen, L., Horne, R. B., & Santolík, O. (2019). Van Allen Probes observations of chorus wave vector orientations: Implications for the chorus-to-hiss mechanism. *Geophysical Research Letters*, *46*(5), 2337–2346. https://doi.org/10.1029/2019GL082111

Hosokawa, K., & Ogawa, Y. (2015). Ionospheric variation during pulsating aurora. *Journal of Geophysical Research: Space Physics*, *120*(7), 5943–5957. https://doi.org/10.1002/2015JA021401

Hua, M., Bortnik, J., Kellerman, A. C., Camporeale, E., & Ma, Q. (2023). Ensemble modeling of radiation belt electron acceleration by chorus waves: Dependence on key input parameters. *Space Weather*, *21*(3). https://doi.org/10.1029/2022SW003234

Hua, M., Bortnik, J., & Ma, Q. (2022). Upper limit of outer radiation belt electron acceleration driven by whistler-mode chorus waves. *Geophysical Research Letters*, *49*(15), e2022GL099618. https://doi.org/10.1029/2022GL099618

Hua, M., Bortnik, J., Spence, H. E., & Reeves, G. D. (2023). Testing the key processes that accelerate outer radiation belt relativistic electrons during geomagnetic storms. *Frontiers in Astronomy and Space Sciences*, *10*, 1168636. https://doi.org/10.3389/fspas.2023.1168636

Isted, G. A., & Millington, G. (1957). The "Dawn Chorus" in radio observations. *Nature*, *180*(4588), 716. https://doi.org/10.1038/180716a0

Jaynes, A. N., Lessard, M. R., Rodriguez, J. V., Donovan, E., Loto'aniu, T. M., & Rychert, K. (2013). Pulsating auroral electron flux modulations in the equatorial magnetosphere. *Journal of Geophysical Research: Space Physics*, *118*(8), 4884–4894. https://doi.org/10.1002/jgra.50434

Jaynes, A. N., Lessard, M. R., Takahashi, K., Ali, A. F., Malaspina, D. M., Michell, R. G., et al. (2015). Correlated Pc4–5 ULF waves, whistler-mode chorus, and pulsating aurora observed by the Van Allen Probes and ground-based systems. *Journal of Geophysical Research: Space Physics*, *120*(10), 8749–8761. https://doi.org/10.1002/2015JA021380

Johnson, R. W. (2001). An introduction to the bootstrap. *Teaching Statistics*, *23*(2), 49–54. https://doi.org/10.1111/1467-9639.00050

Johnstone, A. D. (1978). Pulsating aurora. *Nature*, *274*(5667), 119–126. https://doi.org/10.1038/274119a0

Jones, S. L., Lessard, M. R., Rychert, K., Spanswick, E., & Donovan, E. (2011). Large-scale aspects and temporal evolution of pulsating aurora. *Journal of Geophysical Research*, *116*(A3), A03214. https://doi.org/10.1029/2010JA015840

Kasahara, S., Miyoshi, Y., Yokota, S., Mitani, T., Kasahara, Y., Matsuda, S., et al. (2018). Pulsating aurora from electron scattering by chorus waves. *Nature*, *554*(7692), 337–340. https://doi.org/10.1038/nature25505

Kennel, C. F., & Petschek, H. E. (1966). Limit on stably trapped particle fluxes. *Journal of Geophysical Research*, *71*(1), 1–28. https://doi.org/10.1029/JZ071i001p00001

Kitahara, M., & Katoh, Y. (2019). Anomalous trapping of low pitch angle electrons by coherent whistler mode waves. *Journal of Geophysical Research: Space Physics*, *124*(7), 5568–5583. https://doi.org/10.1029/2019JA026493

Kletzing, C. A., Kurth, W. S., Acuna, M., MacDowall, R. J., Torbert, R. B., Averkamp, T., et al. (2013a). The electric and magnetic field instrument suite and integrated science (EMFISIS) on RBSP. *Space Science Reviews*, *179*(1–4), 127–181. https://doi.org/10.1007/s11214-013-9993-6

Kletzing, C. A., Kurth, W. S., Acuna, M., MacDowall, R. J., Torbert, R. B., Averkamp, T., et al. (2013b). Van Allen probes Emfisis instrument suite [Dataset]. University of Iowa. Retrieved from https://emfisis.physics.uiowa.edu/data/index

Korth, H., Zhang, Y., Anderson, B. J., Sotirelis, T., & Waters, C. L. (2014). Statistical relationship between large-scale upward field-aligned currents and electron precipitation: Current-precipitation relationship. *Journal of Geophysical Research: Space Physics*, *119*(8), 6715–6731. https://doi.org/10.1002/2014JA019961

Kvifte, G., & Pettersen, H. (1969). Morphology of the pulsating aurora. *Planetary and Space Science*, *17*(9), 1599–1607. https://doi.org/10.1016/0032-0633(69)90148-2

Lam, M. M., Horne, R. B., Meredith, N. P., Glauert, S. A., Moffat-Griffin, T., & Green, J. C. (2010). Origin of energetic electron precipitation >30 keV into the atmosphere. *Journal of Geophysical Research*, *115*(A4), A00F08. https://doi.org/10.1029/2009JA014619

Lawrence, D. J., Thomsen, M. F., Borovsky, J. E., & McComas, D. J. (1999). Measurements of early and late time plasmasphere refilling as observed from geosynchronous orbit. *Journal of Geophysical Research*, *104*(A7), 14691–14704. https://doi.org/10.1029/1998ja900087

Lessard, M. R. (2013). A review of pulsating aurora. *Geophysical Monograph Series*, 55–68. https://doi.org/10.1029/2011GM001187

Li, J., Bortnik, J., An, X., Li, W., Angelopoulos, V., Thorne, R. M., et al. (2019). Origin of two-band chorus in the radiation belt of Earth. *Nature Communications*, *10*(1), 4672. https://doi.org/10.1038/s41467-019-12561-3

Li, W., Ma, Q., Thorne, R. M., Bortnik, J., Kletzing, C. A., Kurth, W. S., et al. (2015). Statistical properties of plasmaspheric hiss derived from Van Allen Probes data and their effects on radiation belt electron dynamics. *Journal of Geophysical Research: Space Physics*, *120*(5), 3393–3405. https://doi.org/10.1002/2015JA021048

Li, W., Santolik, O., Bortnik, J., Thorne, R. M., Kletzing, C. A., Kurth, W. S., & Hospodarsky, G. B. (2016). New chorus wave properties near the equator from Van Allen Probes wave observations. *Geophysical Research Letters*, *43*(10), 4725–4735. https://doi.org/10.1002/2016GL068780

Li, W., Thorne, R. M., Bortnik, J., Reeves, G. D., Kletzing, C. A., Kurth, W. S., et al. (2013). An unusual enhancement of low-frequency plasmaspheric hiss in the outer plasmasphere associated with substorm-injected electrons: Amplification of low-frequency HISS. *Geophysical Research Letters*, *40*(15), 3798–3803. https://doi.org/10.1002/grl.50787

Mauk, B., Fox, N. J., Fox, N. J., Kanekal, S., Kessel, R., Sibeck, D. G., & Ukhorskiy, A. Y. (2013). Science objectives and rationale for the radiation belt storm probes mission. *Space Science Reviews*, *179*(1), 3–27. https://doi.org/10.1007/s11214-012-9908-y

Meredith, N. P., Horne, R. B., Johnstone, A. D., & Anderson, R. R. (2000). The temporal evolution of electron distributions and associated wave activity following substorm injections in the inner magnetosphere. *Journal of Geophysical Research*, *105*(A6), 12907–12917. https://doi.org/10.1029/2000JA900010

Meredith, N. P., Horne, R. B., Li, W., Thorne, R. M., & Sicard-Piet, A. (2014). Global model of low-frequency chorus ($f_{lhr} < f < 0.1 f_{ce}$) from multiple satellite observations. *Geophysical Research Letters*, *41*(2), 280–286. https://doi.org/10.1002/2013GL059050

Meredith, N. P., Horne, R. B., Shen, X., Li, W., & Bortnik, J. (2020). Global model of whistler mode chorus in the near-equatorial region (| \lambda $_m$ |< 18°). *Geophysical Research Letters*, *47*(11), e2020GL087311. https://doi.org/10.1029/2020GL087311

Meredith, N. P., Horne, R. B., Sicard-Piet, A., Boscher, D., Yearby, K. H., Li, W., & Thorne, R. M. (2012). Global model of lower band and upper band chorus from multiple satellite observations. *Journal of Geophysical Research*, *117*(A10), A10225. https://doi.org/10.1029/2012JA017978

Meredith, N. P., Horne, R. B., Thorne, R. M., & Anderson, R. R. (2009). Survey of upper band chorus and ECH waves: Implications for the diffuse aurora. *Journal of Geophysical Research*, *114*(A7), A07218. https://doi.org/10.1029/2009JA014230

Miyoshi, Y., Hosokawa, K., Kurita, S., Oyama, S.-I., Ogawa, Y., Saito, S., et al. (2021). Penetration of MeV electrons into the mesosphere accompanying pulsating aurorae. *Scientific Reports*, *11*(1), 13724. https://doi.org/10.1038/s41598-021-92611-3

Miyoshi, Y., Saito, S., Kurita, S., Asamura, K., Hosokawa, K., Sakanoi, T., et al. (2020). Relativistic electron microbursts as high-energy tail of pulsating aurora electrons. *Geophysical Research Letters*, *47*(21), e2020GL090360. https://doi.org/10.1029/2020GL090360

Newell, P. T., & Gjerloev, J. W. (2011). Evaluation of SuperMAG auroral electrojet indices as indicators of substorms and auroral power. *Journal of Geophysical Research*, *116*(A12), 2011JA016779. https://doi.org/10.1029/2011JA016779

Ni, B., Thorne, R. M., Shprits, Y. Y., & Bortnik, J. (2008). Resonant scattering of plasma sheet electrons by whistler-mode chorus: Contribution to diffuse auroral precipitation. *Geophysical Research Letters*, *35*(11), L11106. https://doi.org/10.1029/2008GL034032

Nishimura, Y., Bortnik, J., Li, W., Thorne, R. M., Chen, L., Lyons, L. R., et al. (2011). Multievent study of the correlation between pulsating aurora and whistler mode chorus emissions. *Journal of Geophysical Research*, *116*(A11), A11221. https://doi.org/10.1029/2011JA016876

Nishimura, Y., Bortnik, J., Li, W., Thorne, R. M., Lyons, L. R., Angelopoulos, V., et al. (2010). Identifying the driver of pulsating aurora. *Science*, *330*(6000), 81–84. https://doi.org/10.1126/science.1193186

Oguti, T. (1976). Recurrent auroral patterns. *Journal of Geophysical Research*, *81*(10), 1782–1786. https://doi.org/10.1029/JA081i010p01782

Oguti, T., Kokubun, S., Hayashi, K., Tsuruda, K., Machida, S., Kitamura, T., et al. (1981). Statistics of pulsating auroras on the basis of all-sky TV data from five stations. I. Occurrence frequency. *Canadian Journal of Physics*, *59*(8), 1150–1157. https://doi.org/10.1139/p81-152

Oyama, S., Kero, A., Rodger, C. J., Clilverd, M. A., Miyoshi, Y., Partamies, N., et al. (2017). Energetic electron precipitation and auroral morphology at the substorm recovery phase. *Journal of Geophysical Research: Space Physics*, *122*(6), 6508–6527. https://doi.org/10.1002/2016JA023484

Partamies, N., Tesema, F., & Bland, E. (2022). Appearance and precipitation characteristics of high-latitude pulsating aurora. *Frontiers in Astronomy and Space Sciences*, *9*, 923396. https://doi.org/10.3389/fspas.2022.923396

Rodger, C. J., Hendry, A. T., Clilverd, M. A., Forsyth, C., & Morley, S. K. (2022). Examination of radiation belt dynamics during substorm clusters: Activity drivers and dependencies of trapped flux enhancements. *Journal of Geophysical Research: Space Physics*, *127*(1), e2021JA030003. https://doi.org/10.1029/2021JA030003

Roederer, J. G. (1970). *Dynamics of geomagnetically trapped radiation* (Vol. 2). Springer Berlin Heidelberg. https://doi.org/10.1007/978-3-642-49300-3

Schroeder, J. W. R., Howes, G. G., Kletzing, C. A., Skiff, F., Carter, T. A., Vincena, S., & Dorfman, S. (2021). Laboratory measurements of the physics of auroral electron acceleration by Alfvén waves. *Nature Communications*, *12*(1), 3103. https://doi.org/10.1038/s41467-021-23377-5

Sheeley, B. W., Moldwin, M. B., Rassoul, H. K., & Anderson, R. R. (2001). An empirical plasmasphere and trough density model: CRRES observations. *Journal of Geophysical Research*, *106*(A11), 25631–25641. https://doi.org/10.1029/2000JA000286

Spence, H. E., Reeves, G. D., Baker, D. N., Blake, J. B., Bolton, M., Bourdarie, S., et al. (2013). Science goals and overview of the radiation belt storm probes (RBSP) energetic particle, composition, and thermal plasma (ECT) suite on NASA's Van Allen Probes mission. *Space Science Reviews*, *179*(1–4), 311–336. https://doi.org/10.1007/s11214-013-0007-5

Summers, D., Thorne, R. M., & Xiao, F. (1998). Relativistic theory of wave-particle resonant diffusion with application to electron acceleration in the magnetosphere. *Journal of Geophysical Research*, *103*(A9), 20487–20500. https://doi.org/10.1029/98JA01740

Tesema, F., Partamies, N., Tyssøy, H. N., Kero, A., & Smith-Johnsen, C. (2020). Observations of electron precipitation during pulsating aurora and its chemical impact. *Journal of Geophysical Research: Space Physics*, *125*(6), e2019JA027713. https://doi.org/10.1029/2019JA027713

Trakhtengerts, V. Y., Demekhov, A. G., Titova, E. E., Kozelov, B. V., Santolik, O., Gurnett, D., & Parrot, M. (2004). Interpretation of Cluster data on chorus emissions using the backward wave oscillator model. *Physics of Plasmas*, *11*(4), 1345–1351. https://doi.org/10.1063/1.1667495

Troyer, R. N., Jaynes, A. N., Kaeppler, S. R., Varney, R. H., Reimer, A. S., & Jones, S. L. (2022). Substorm activity as a driver of energetic pulsating aurora. *Frontiers in Astronomy and Space Sciences*, *9*. https://doi.org/10.3389/fspas.2022.1032552

Tsurutani, B. T., & Smith, E. J. (1974). Postmidnight chorus: A substorm phenomenon. *Journal of Geophysical Research*, *79*(1), 118–127. https://doi.org/10.1029/JA079i001p00118

Turunen, E., Kero, A., Verronen, P. T., Miyoshi, Y., Oyama, S., & Saito, S. (2016). Mesospheric ozone destruction by high-energy electron precipitation associated with pulsating aurora. *Journal of Geophysical Research: Atmospheres*, *121*(19), 11852–11861. https://doi.org/10.1002/2016JD025015

Verronen, P. T., Kero, A., Partamies, N., Szelag, M. E., Oyama, S.-I., Miyoshi, Y., & Turunen, E. (2021). Simulated seasonal impact on middle atmospheric ozone from high-energy electron precipitation related to pulsating aurorae. *Annales Geophysicae*, *39*(5), 883–897. https://doi.org/10.5194/angeo-39-883-2021

Wygant, J. R., Bonnell, J. W., Goetz, K., Goetz, K., Ergun, R., Mozer, F. S., et al. (2013). *The electric field and waves instruments on the radiation belt storm probes mission*. Springer US. https://doi.org/10.1007/s11214-013-0013-7